machines

MDPI

Article

Nonlinear Analysis of Rotor-Bearing-Seal System with Varying Parameters Muszynska Model Based on CFD and RBF

Rui Wang [1,2,*], Yuefang Wang [2], Xiaojian Cao [3], Shuhua Yang [1] and Xinglin Guo [2]

[1] Shenyang Blower Works Group Corporation, Shenyang 110089, China
[2] Department of Engineering Mechanics, Dalian University of Technology, Dalian 116024, China
[3] College of Pipeline and Civil Engineering, China University of Petroleum (East China), Qingdao 266580, China
* Correspondence: wangruiauthor@aliyun.com

Abstract: The computational fluid dynamics (CFD) combined with radial basis function (RBF) method were adopted to obtain the response surface of the Muszynska nonlinear seal force model coefficient with two variables: eccentricity and rotation speed. During the implementation of the simulation, three coefficients of the seal force model were calculated in each sub-step according to the current state of the rotor-bearing seal system; following which the rotor dynamics analysis with varying parameters was realized. As with the traditional constant coefficient method, the first-order critical speed of the system was obtained, and the bifurcation point and oil film whirl of the system response were identified. The difference is that the coefficients of the traditional method ordinarily do not change with the state of the system. Comparing the results of the varying parameter method with those of the traditional method, it can be seen that the speeds of the system corresponding to the bifurcation and oil film whirl are different. The varying parameter rotor dynamics simulation method proposed in this paper provides a new way of analyzing the nonlinear characteristics of rotor-bearing-seal systems.

Keywords: Muszynska nonlinear seal force model; computational fluid dynamics; radial basis function; bifurcation; oil film whirl; first-order critical speed

Citation: Wang, R.; Wang, Y.; Cao, X.; Yang, S.; Guo, X. Nonlinear Analysis of Rotor-Bearing-Seal System with Varying Parameters Muszynska Model Based on CFD and RBF. *Machines* **2022**, *10*, 1238. https://doi.org/10.3390/machines10121238

Academic Editor: Davide Astolfi

Received: 14 November 2022
Accepted: 14 December 2022
Published: 18 December 2022

1. Introduction

According to the literature [1–3], annular seals have strong effects on the rotors due to the squeeze action with turbulent flow. The rotor dynamic characteristics of rotor-bearing-seal systems primarily depend on the dynamics of the bearings and seals. In most cases, the flow of fluid in seals is a complex three-dimensional turbulence. The fluid in seals rotates with the rotor; moreover, due to eccentricity of the rotor, the distribution of circumferential pressure is uneven. In some cases, such as when the rotational speed of the rotor exceeds the unstable speed of the seal, the fluid in seals will excite the rotor and may cause a strong self-excited vibration of the rotor. This type of phenomenon has occurred in the rotational machinery in electric power, the petrochemical industry, and so on. Prediction of seal stability is of great significance for the design of rotor systems. The numerical simulation method is an economical and effective approach for predicting seal stability. The adoption of an accurate seal force model is the key to the numerical method. For this purpose, much research has been carried out.

Black [1] proposed a linear seal force model based on short bearing theory. The stability of the centrifugal pump rotor was investigated due to certain seal parameters, such as inlet loss coefficient, axial flow velocity, radial clearance and friction coefficient. Childs [2,3] applied the Hirs's turbulent lubrication equations and perturbation method to improve Black's model. Following that, Childs [4–6] presented both a one-control and two-control volume model for labyrinth seals and used CFD and experiments to study the rotordynamics of a negative swirl brake for a tooth-on-stator labyrinth seal. Nelson [7] applied Hirs's and Moody's equations to investigate the rotordynamic coefficients of annular pressure seals with compressible and incompressible flows, respectively. Moreover, the values of stiffness, cross stiffness, damping and cross damping with relative roughness of the seals were obtained. Based on many experiments, Muszynska and Bently [8–10] proposed a seal-fluid force model with clear physical meaning to represent the nonlinear behavior of seal-fluid dynamic force. The fluid circumferential average velocity of the flow was employed to construct the dynamic coefficients of the model. Since the main mechanical characteristics of the seal force were taken into account, the Muszynska nonlinear seal force model has been widely used.

The numerical method has also been used to investigate the nonlinear dynamic behavior of a rotor-seal system. Various phenomena of the system, such as periodic motion, double-periodic motion and quasi-periodic motion were obtained [11]. The seal force model was adopted by Wang et al. [12] in their study on bifurcation and periodic motion of a symmetric rotor-seal system. The Timoshenko beam element and Muszynska seal force model were employed by Zhang to simulate a rotor-bearing-labyrinth seal system [13]. Xu [14] conducted research into the stability of rotor/seal systems with dynamic vibration absorbers. The dynamic characteristics of annular seals under large eccentricities were investigated by the transient CFD simulation [15]. The surrogate model was applied to the parametric design of a rotor-seal system by Mutra [16]. With the development of computer technology, the CFD method was introduced into the analysis of the fluid field in seals. The application of this method can efficiently yield the characteristics of seal fluid. Furthermore, the results of the CFD simulation can be used not only to analyze the dynamic behavior of the seal, but also show good correlation with experimental data [17,18]. Luo [19] used numerical and experimental methods to exhibit the dynamic characteristics of a seal-rotor system with rub-impact fault.

In fact, the parameters of rotor systems changed with the operation of turbomachinery. In order to investigate the dynamic characteristics of a rotor system with bearings and seals, nonlinear models of bearings and seals must be employed. In the traditional simulation process, the parameters of the seal model are constants; whereas the parameters of the seal change according to states, such as rotational speed and eccentricity of the rotor. Therefore, the varying parameters of the seal model should be applied to perform the numerical simulation.

The Muszynska seal force model was employed to represent the ring seal of a centrifugal pump in this paper. The CFD method was used to simulate the fluid flow of the ring seal with six relative eccentricities and five rotational speeds, making 30 cases in total. The parameters for the Muszynska model are obtained. The RBF method is applied to fit the approximate function surfaces of the three parameters of the seal model. At each step of the numerical simulation, the values of the three functions are identified according to the results of eccentricity and rotational speed, correspondingly. The results prove that the varying parameters method employed in this paper achieve more accurate simulation than the traditional method.

2. The Muszynska Nonlinear Seal Force Model

Based on the literature [8–10], the fluid in bearings or seals is dragged by viscous friction into circumferential motion by rotor rotation. The fluid force and its circumferential flow play an appreciable role in the resulting dynamic phenomena and have, therefore, a significant effect on rotor dynamic behavior. Muszynska [8] proposed the nonlinear seal force model, which takes into account the effect of circumferential flow in seals, and the formula can be expressed by Equation (1).

$$\begin{Bmatrix} F_{XS} \\ F_{YS} \end{Bmatrix} = -\begin{bmatrix} K - M_f\Omega^2\tau^2 & \Omega D\tau \\ -\Omega D\tau & K - M_f\Omega^2\tau^2 \end{bmatrix}\begin{Bmatrix} X_1 \\ Y_1 \end{Bmatrix} - \begin{bmatrix} D & 2M_f\Omega\tau \\ -2M_f\Omega\tau & D \end{bmatrix}\begin{Bmatrix} \dot{X}_1 \\ \dot{Y}_1 \end{Bmatrix} - \begin{bmatrix} M_f & 0 \\ 0 & M_f \end{bmatrix}\begin{Bmatrix} \ddot{X}_1 \\ \ddot{Y}_1 \end{Bmatrix} \tag{1}$$

where K is equivalent stiffness; M_f is equivalent mass; D is equivalent damping; Ω is rotational speed; τ, K, D can be written by Equation (2).

$$\begin{cases} \tau = \tau_0(1-\varepsilon)^b \\ K = K_0(1-\varepsilon^2)^{-n_1} \\ D = D_0(1-\varepsilon^2)^{-n_2} \end{cases} \tag{2}$$

where τ_0 is the average angular speed for the unperturbed rotor; b is empirical coefficient; $\varepsilon = \sqrt{x^2+y^2}/C$ is relative eccentricity; C is the radial clearance of the seal; $n_1 = -3$ and $n_2 = -2$ [9]. K_0, D_0 and M_f are given by Equation (3) in accordance with [2].

$$\begin{gathered} K_0 = \mu_0\mu_3 \\ D_0 = \mu_1\mu_3 T \\ M_f = \mu_2\mu_3 T^2 \end{gathered} \tag{3}$$

where

$\mu_0 = 2\sigma^2 E(1-m_0)/(1+z+2\sigma)$;
$\mu_1 = 2\sigma^2[E/\sigma + B(1/6+E)/2]/(1+z+2\sigma)$;
$\mu_2 = \sigma(1/6+E)/(1+z+2\sigma)$;
$\mu_3 = \pi R\Delta P/\lambda$;
$\lambda = n_0 R_a^{m_0}[1+(R_v/R_a)^2]^{\frac{1+m_0}{2}}$;
$T = L/v_z$;
$B = 2 - ((R_v/R_a)^2 - m_0)/((R_v/R_a)^2+1)$;
$E = (1+z)/[2(1+z+2\sigma)]$;
$R_v = R\Omega C/v$;
$R_a = 2v_z C/v$;
$\sigma = \lambda L/C$;

$n_0 = 0.079$ and $m_0 = -0.25$ are coefficients for Hirs's turbulence equations; z is inlet loss coefficient; ΔP is pressure drop; R_v is circumferential Reynolds number; R_a is axial Reynolds number; v_z is axial velocity; v is kinetic viscosity; λ is friction loss coefficient; L is length of seal or width of seal tooth.

The seal force, which is generated by the Muszynska model, is variable with the eccentricity of the rotor in the references. However, two parameters in these papers, i.e., inlet loss coefficient (z) and axial velocity (v_z), are constant during the simulation process. According to Equation (3), these two parameters of the model are functions of eccentricity and rotational speed. Furthermore, τ is computed by empirical Equation (2) in these papers. In fact, τ is also a function of eccentricity and rotational speed. For the reasons mentioned above, inlet loss coefficient, axial velocity and fluid circumferential average velocity ratio should be written as functions of eccentricity and rotational speed.

3. CFD Simulation

The research objects of this paper were the ring seals of a centrifugal pump. The locations of the seals are shown in Figure 1a,b and its local enlarged drawing is shown in Figure 1c. The impeller in Figure 1a,b is shown in red, the ring seals are shown in blue and the guide vane is shown in orange. The 3D model of the seal fluid is shown in Figure 1d.

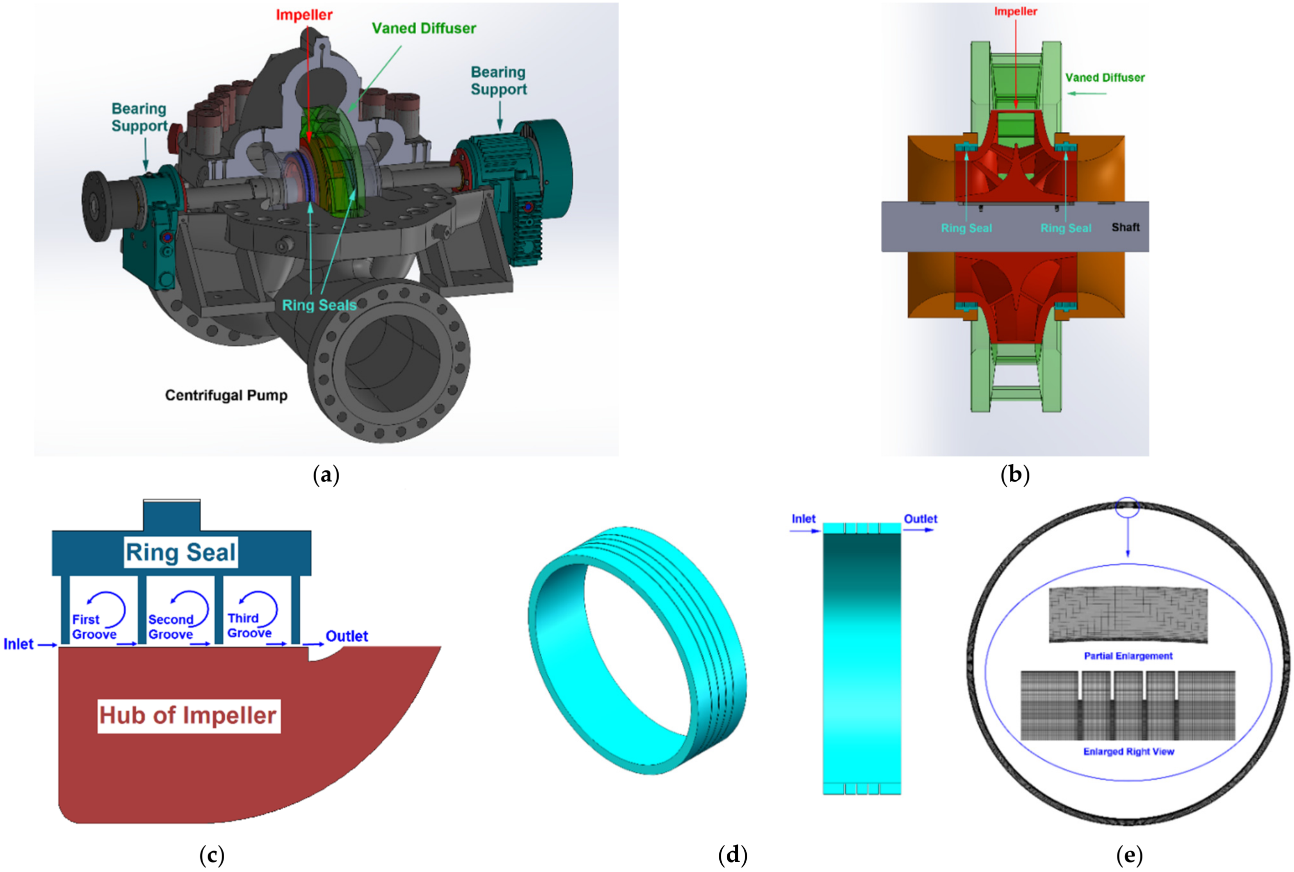

Figure 1. (**a**) The centrifugal pump; (**b**) The ring seals, impeller and vaned diffuser; (**c**) Flow in the seal; (**d**) 3D model of flow domain; (**e**) CFD mesh.

The CFD method is applied to obtain the fluid parameters of the Muszynska nonlinear seal force model. The fluid is water, and it is regarded as an incompressible fluid during the CFD process. In the Cartesian coordinate system, the tensor form of the Navier−Stokes equation for incompressible fluids is as follows:

$$\rho \frac{\mathrm{D}u_i}{\mathrm{D}t} = \rho f_i - \frac{\partial p}{\partial x_i} + \mu \frac{\partial u_i}{\partial x_j \cdot \partial x_j} (i, j = 1, 2, 3) \tag{4}$$

where ρ is fluid density; u_i (i = 1,2,3) are velocity component; $\frac{D}{Dt} = \frac{\partial}{\partial t} + (V \cdot \nabla)$; ρf_i is volume force; p is pressure; μ is dynamic viscosity. With the operation of the pump, the fluid in the ring seal is fully developed turbulent flow. The k-ω Shear Stress Transport (SST) model [20] is employed to perform the CFD simulations. The kinetic energy equation and the dissipation equation are listed below, and the meaning of the characters in the formula can refer to reference [20].

$$\frac{\partial k}{\partial t} + \frac{\partial \rho u_j k}{\partial x_j} = \tau_{ij} \frac{\partial u_i}{\partial x_j} - \beta^* \rho \omega K + \frac{\partial}{\partial x_j} \left[(\mu + \sigma_k \mu_t) \frac{\partial k}{\partial x_j} \right] \tag{5}$$

$$\frac{\partial \rho \omega}{\partial t} + \frac{\partial \rho u_j \omega}{\partial x_j} = \frac{\gamma}{v_t} \tau_{ij} \frac{\partial u_j}{\partial x_j} - \beta \rho \omega^2 + \frac{\partial}{\partial x_j} \left[(\mu + \sigma_\omega \mu_t) \frac{\partial \omega}{\partial x_j} \right] + \frac{2\rho(1 - F_1)\sigma_{\omega 2}}{\omega} \frac{\partial k}{\partial x_j} \frac{\partial \omega}{\partial x_j} \tag{6}$$

The axial view and side view of the mesh for the seal are shown in Figure 1e. Both the cutaway view of hexahedral mesh of the fluid and the size of the seal are shown in Figure 2. According to Figure 2, the total number of nodes is 14,002,224 and the total number of elements is 13,365,300; S = 4 mm is the length and height of the seal groove; L = 0.5 mm is the width of the seal tooth; C = 0.4 mm is the radial clearance of the seal; R = 100 mm is the radius of impeller ring.

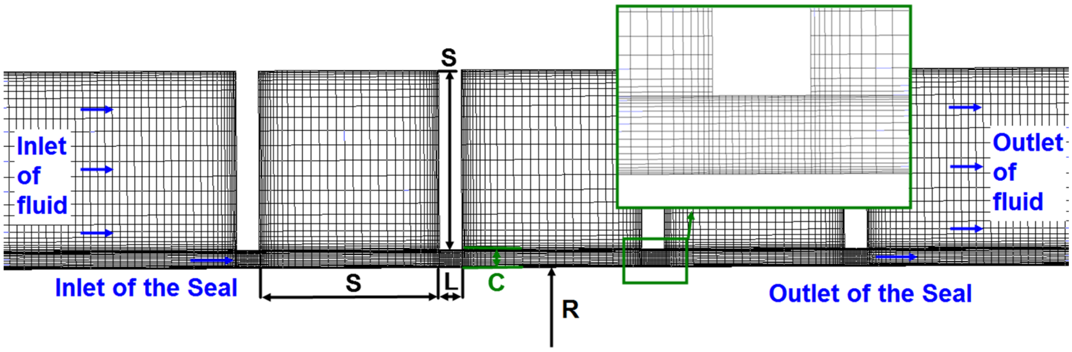

Figure 2. The mesh of fluid and the size of the seal.

Ansys CFX software was used to perform the simulations. There were six 3D-models with relative eccentricities ε = 0, 0.1, 0.3, 0.5, 0.7 and 0.9, respectively; and there were six meshes for the six 3D-models, correspondingly. The rotational speeds were 900 rpm, 4300 rpm, 7700 rpm, 11,100 rpm and 14,500 rpm, respectively. The rotational speeds were installed on faces that were interfaces of the ring seal and the impeller. The fluid in the seal is water. The attributes of water are the default values of the CFX software. The boundary conditions of the flow field are listed in Table 1. The simulation results of the case of relative eccentricity 0.3 with rotational speed 7700 rpm are illustrated in Figure 3.

Table 1. The boundary conditions.

Inlet		Outlet
Pressure 0.9 MPa	Axial Velocity 10 m/s	Pressure 0.4 MPa

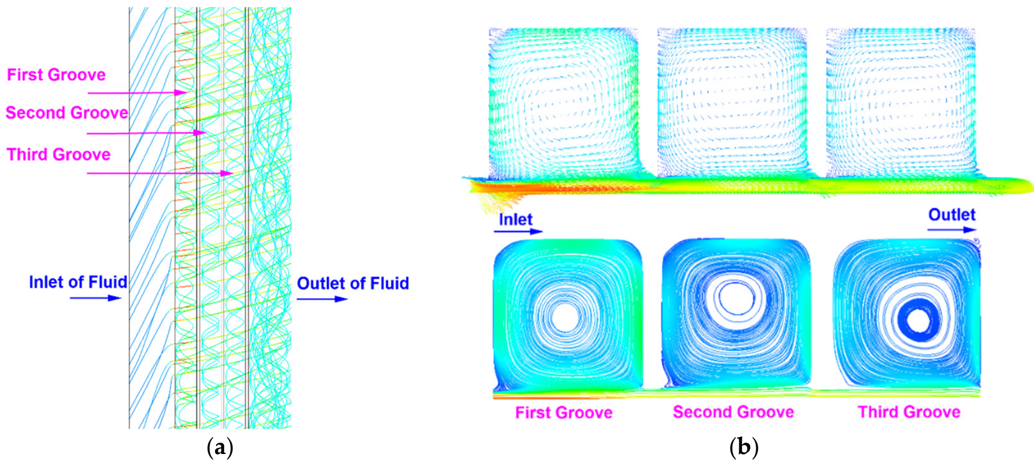

Figure 3. (**a**) 3D streamline diagram; (**b**) Vector diagram and streamline diagram of fluid field.

Due to the combined effect of the rotational speed and the pressure difference between the inlet and the outlet, the three-dimensional flow line is spiral in the ring seal, as in the results shown in Figure 3. This phenomenon is similar to [17,21]. The results of the average value of fluid axial speed, inlet loss coefficient, and average value of tangential speeds of fluid and fluid circumferential average velocity ratio of the ring seal are shown in Figures 4–7.

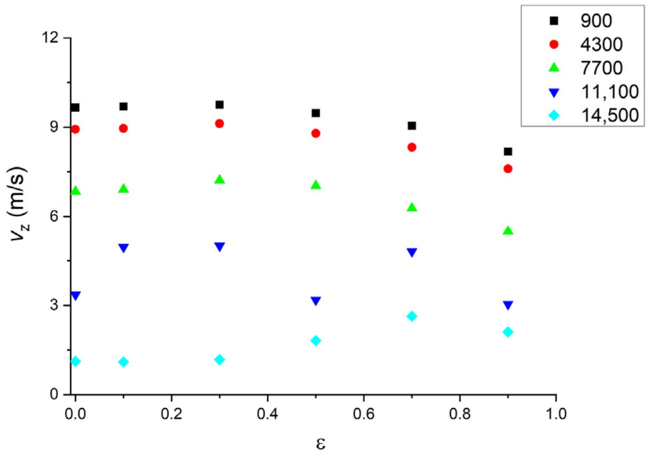

Figure 4. Average value of fluid axial speeds (v_z) of ring seal (Unit: m/s).

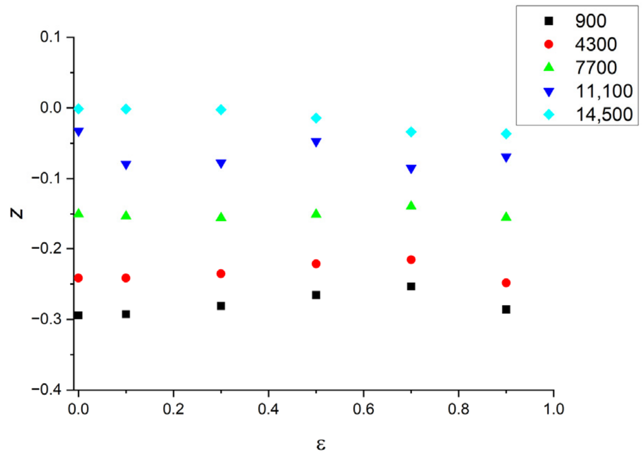

Figure 5. Inlet loss factor (z) of ring seal.

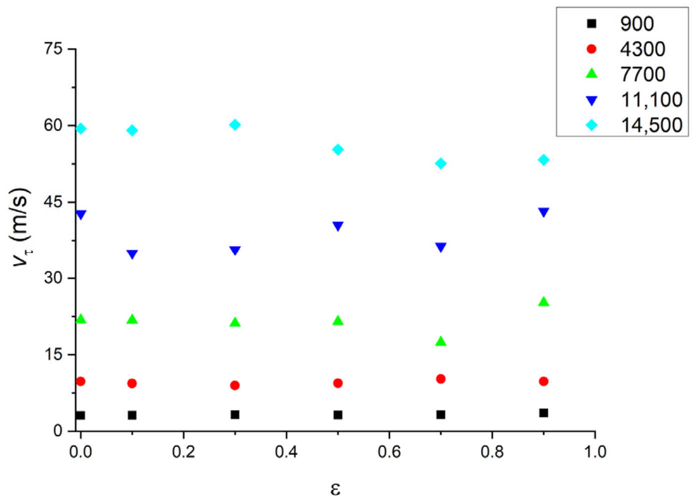

Figure 6. Average value of tangential speeds (v_τ) of fluid (Unit: m/s).

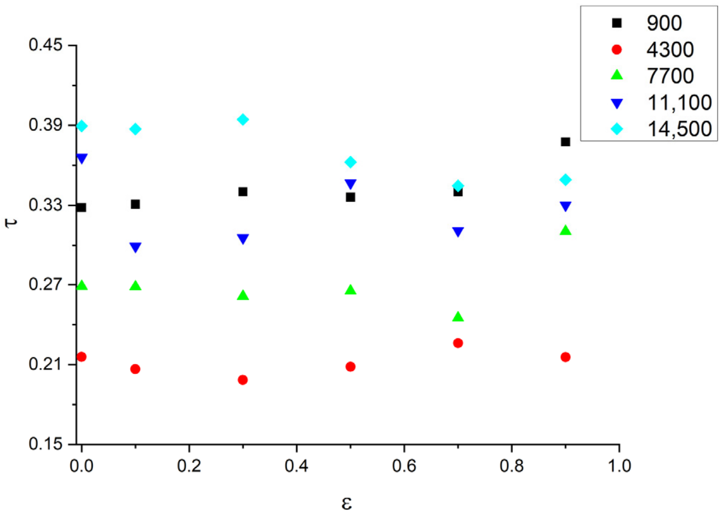

Figure 7. Fluid circumferential average velocity ratio ($\tau = v_\tau/\Omega$) of fluid.

Based on the results in Figures 4–7, we can conclude that: (1) with increase in rotational speed, the average value of the axial speeds and the inlet loss factor of the seal are gradually reduced; (2) with increase in the rotational speed, the average value of the tangential speeds of the seal gradually increases. Because the increasing trend is not linear, the average velocity ratio of tangential speed does not increase with the increase in rotational speed, but rather presents a nonlinear distribution.

The data in Figures 4–7 are scattered point sets. The results of the references [22,23] show that the RBF method is effective in dealing with scattered data. The RBF method is used to synthesize these scattered point sets into approximate function surfaces with relative eccentricity and dimensionless speed ($\omega = \Omega/14{,}500$) as variables, respectively.

4. The Response Surface by RBF

There are n scattered points $\{p_1, p_2, \cdots, p_n\}$, and each point has a corresponding constraint value $\{h_1, h_2, \cdots, h_n\}$. As f:$R_n \to R$, for every scattered point, the constraint can be satisfied by the following formula:

$$f(p_i) = h_i,\ i = 1,2\ldots,n \tag{7}$$

As the resulting surface is as smooth and continuous as possible, the general form of the RBF is:

$$f(p) = \sum_{i=1}^{n} \lambda_i \phi(\|p - p_i\|),\ i = 1,2,\ldots,n \tag{8}$$

where p represents any data point on the surface; λ_i is the evaluation variable of the weighted value of each radial benchmark; $\|p - p_i\|$ is the Euclidean distance; and $\phi(\|p - p_i\|) = r^k = \|p_i - p_i\|^k$ is a positive definite basis function.

The data in Figures 4–7 are used as sample points, and the approximate function surface with relative eccentricity and dimensionless speed ($\omega = \Omega/14{,}500$) as variables is fitted by the radial basis function method, as shown in Figure 8.

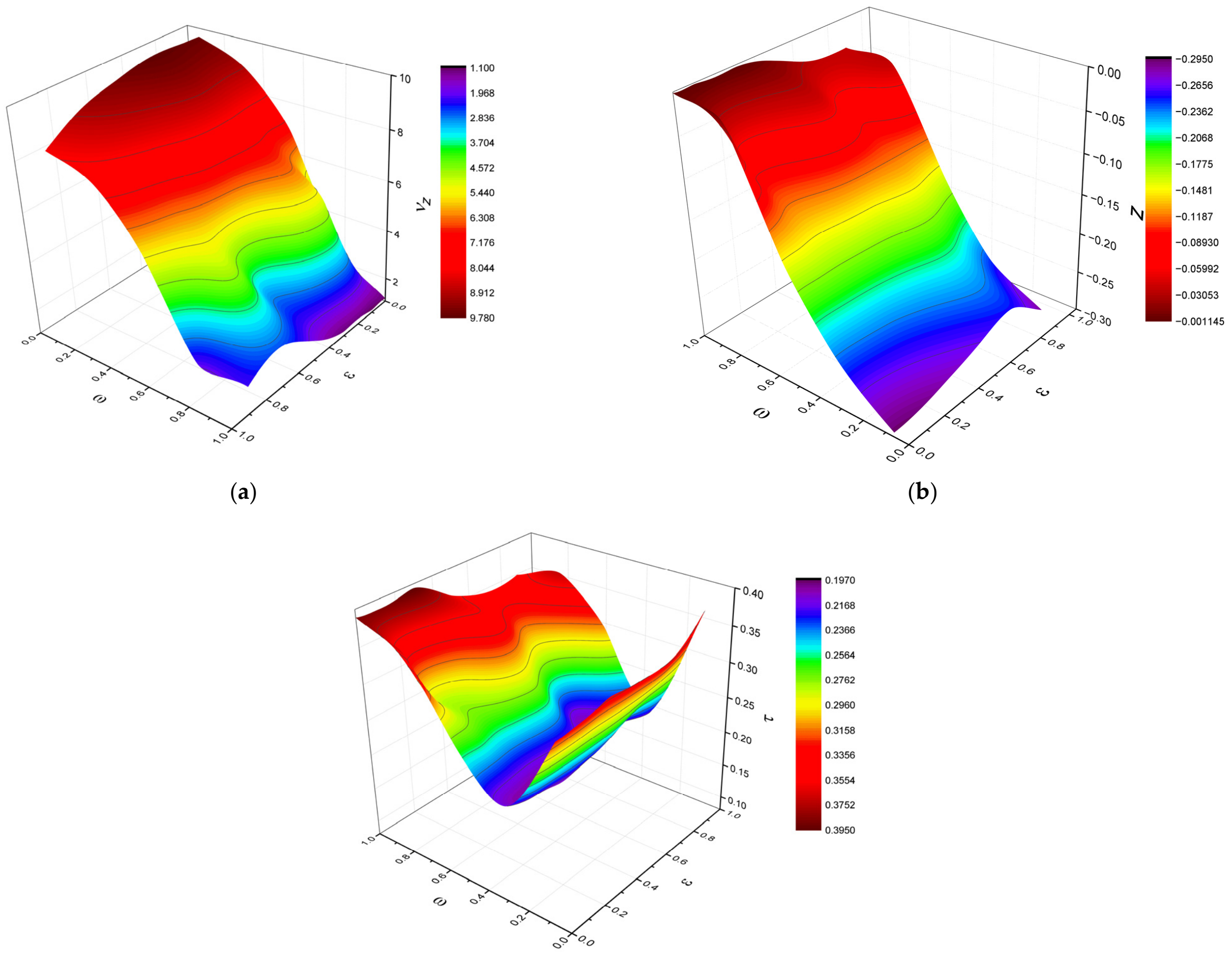

(**a**) (**b**)

(**c**)

Figure 8. Approximate function surfaces: (**a**) Average value of axial speeds; (**b**) Inlet loss factor; (c) Factors of average angular speed.

5. Rotor Dynamics Analysis of Varying Parameters

5.1. Numerical Model and Governing Equations

The centrifugal pump rotor-bearing-seal system was simplified as a numerical model of three concentrated masses, equivalent stiffness, nonlinear bearing force model [24] and nonlinear seal force model, as shown in Figure 9.

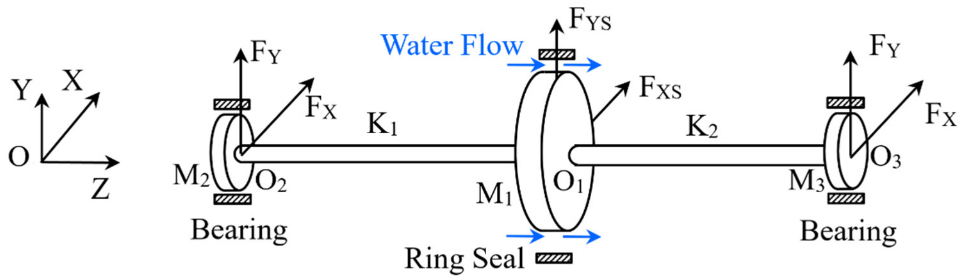

Figure 9. Model of the rotor-bearing-seal system.

The differential equation of motion of a system is:

$$\begin{cases} M_1\ddot{X}_1 + D_1\dot{X}_1 + K_1(X_1 - X_2) + K_2(X_1 - X_3) = F_{XS} + M_1\Omega^2 E_1\cos(\Omega t) \\ M_1\ddot{Y}_1 + D_1\dot{Y}_1 + K_1(Y_1 - Y_2) + K_2(Y_1 - Y_3) = F_{YS} - M_1 g + M_1\Omega^2 E_1\sin(\Omega t) \\ M_2\ddot{X}_2 + D_2\dot{X}_2 + K_1(X_2 - X_1) = F_X\left(X_2, Y_2, \dot{X}_2, \dot{Y}_2\right) \\ M_2\ddot{Y}_2 + D_2\dot{Y}_2 + K_1(Y_2 - Y_1) = F_Y\left(X_2, Y_2, \dot{X}_2, \dot{Y}_2\right) - M_2 g \\ M_3\ddot{X}_3 + D_3\dot{X}_3 + K_2(X_3 - X_1) = F_X\left(X_3, Y_3, \dot{X}_3, \dot{Y}_3\right) \\ M_3\ddot{Y}_3 + D_3\dot{Y}_3 + K_2(Y_3 - Y_1) = F_Y\left(X_3, Y_3, \dot{X}_3, \dot{Y}_3\right) - M_3 g \end{cases} \tag{9}$$

The dimensionless form is:

$$\begin{cases} \ddot{x}_1 + \frac{D_1+D}{m_1\Omega}\dot{x}_1 + \frac{2M_f\tau}{m_1}\dot{y}_1 + \frac{k_1}{m_1\Omega^2}x_1 - \frac{c}{m_1\Omega^2 C}(K_1x_2 + K_2x_3) + \frac{D\tau}{m_1\Omega}y_1 = e_1\cos(\Omega t) \\ \ddot{y}_1 + \frac{D_1+D}{m_1\Omega}\dot{y}_1 - \frac{2M_f\tau}{m_1}\dot{x}_1 + \frac{k_1}{m_1\Omega^2}y_1 - \frac{c}{m_1\Omega^2 C}(K_1y_2 + K_2y_3) - \frac{D\tau}{m_1\Omega}x_1 = e_1\sin(\Omega t) - \overline{g} \\ \ddot{x}_2 + d_2\dot{x}_2 + k_{12}\left(x_2 - \frac{C}{c}x_1\right) = N_2 f_x(x_2, y_2, \dot{x}_2, \dot{y}_2) \\ \ddot{y}_2 + d_2\dot{y}_2 + k_{12}\left(y_2 - \frac{C}{c}y_1\right) = N_2 f_y(x_2, y_2, \dot{x}_2, \dot{y}_2) - \overline{g} \\ \ddot{x}_3 + d_3\dot{x}_3 + k_{23}\left(x_3 - \frac{C}{c}x_1\right) = N_3 f_x(x_3, y_3, \dot{x}_3, \dot{y}_3) \\ \ddot{y}_3 + d_3\dot{y}_3 + k_{23}\left(y_3 - \frac{C}{c}y_1\right) = N_3 f_y(x_3, y_3, \dot{x}_3, \dot{y}_3) - \overline{g} \end{cases} \tag{10}$$

where $x_1 = X_1/(\Omega^2 C)$; $y_1 = Y_1/(\Omega^2 C)$; $\dot{x}_1 = \dot{X}_1/(\Omega C)$; $\dot{y}_1 = \dot{Y}_1/(\Omega C)$; $\ddot{x}_1 = \ddot{X}_1/C$; $\ddot{y}_1 = \ddot{Y}_1/C$; $m_1 = M_1 + M_f$; $k_1 = K - M_f\Omega^2\tau^2 + K_1 + K_2$; $e_1 = M_1E_1/(m_1C)$; $\overline{g} = M_1 g/(m_1\Omega^2 C)$; $d_i = D_i/(M_i\Omega)$ (i = 2,3); $k_{ij} = K_i/(M_j\Omega^2)$ (i = 1,2; j = 2,3); $N_i = sP/\left(M_i c\Omega^2\right)$ (i = 2,3); $f_x = F_X/sP$; $f_y = F_Y/sP$; Sommerfeld number $s = \Omega\mu Rl(R/c)^2(l/2R)^2/P$; X_1, X_2 and X_3 are horizontal direction displacements; x_1, x_2 and x_3 are dimensionless horizontal direction displacements; Y_1, Y_2 and Y_3 are gravity direction displacements; y_1, y_2 and y_3 are dimensionless gravity direction displacements; c is radial clearance of bearing; D, D_1, D_2 and D_3 are equivalent damping; E_1 is eccentricity; F_X and F_Y are nonlinear bearing force; F_{XS} and F_{YS} are nonlinear seal force; K_1 and K_2 are shaft equivalent stiffness; l is length of bearing; M_1, M_2 and M_3 are mass; P = (M_1 + M_2 + M_3)g/2; M_f is equivalent mass; t is time; μ is dynamic viscosity. The subscripts (1,2,3) are the locations of impeller, left bearings and right bearings, respectively. The superscripts '$\cdot$' and '$\cdot\cdot$' are $\partial/\partial t$ and $\partial^2/\partial t^2$, respectively.

It can be seen from Formulas (1)–(3) that the coefficients of the Muszynska model are closely related to the three variables, which are the fluid axial velocity, the inlet loss coefficient, and the fluid circumferential velocity ratio. In the traditional numerical simulation process, the first two (v_z and λ) adopt the constant value, while the latter (τ) adopts the empirical formula. In the process of rotor operation, these three variables are closely related to the flow field state (e.g., eccentricity and rotational speed) and are all transient variables. Based on the RBF method, the relative eccentricity and dimensionless rotational speed are used as variables, which are assisted by the CFD method to calculate the finite sample points, and then generate the approximate function surfaces of the three variables mentioned above. In each sub-step of the calculation process, the corresponding values of the approximate function surfaces are taken and substituted into the motion equations to solve. In this paper, the method with varying parameters (VP) is written according to the VP method.

5.2. Comparing the Rotor Dynamic Characteristics of the VP Method to the Traditional method

The nonlinear method is used to analyze the results. The bifurcation maps of the dimensionless displacement amplitude at the rotor and bearing by the VP method are shown in Figure 10.

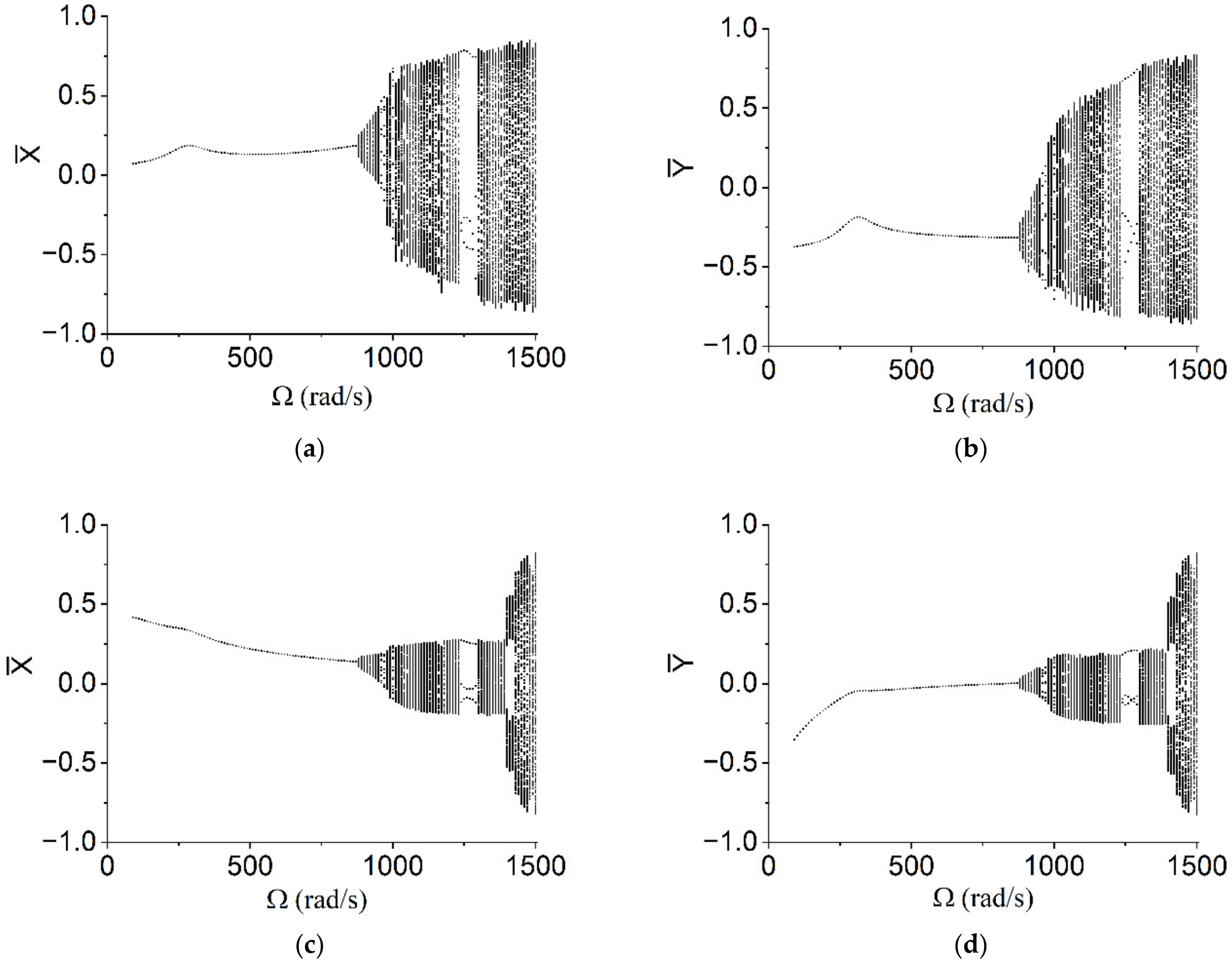

Figure 10. The bifurcation maps of displacements of the VP method: (**a**) X-displacement of rotor; (**b**) Y-displacement of rotor; (**c**) X-displacement of bearing; (**d**) Y-displacement of bearing.

The following conclusions can be seen from Figure 10:

(1) When $\Omega \in [90, 300]$ rad/s, the amplitude of the rotor increases gradually. Following this, with the increase in rotational speed, the amplitude of the rotor decreases gradually. It can be identified that ω_n = 300 rad/s is the first-order critical speed of the rotor system;

(2) When $\Omega \in [880, 1390]$ rad/s, the bifurcation has been observed and the amplitude value increases;

(3) When $\Omega \geq 1400$ rad/s, the amplitude of the bearing increases again substantially, with the maximum close to value 1.

In the traditional method, the inlet loss coefficient and the axial flow velocity are generally constant, and the circumferential average velocity ratio is generally an empirical formula [11,12,23]. The parameters are v_z = 5 m/s, $z = -0.15$, $\tau_0 = 0.35$ when there is no disturbance and $b = 0.12$. The bifurcation maps of the dimensionless displacement amplitude at the rotor and bearing are shown in Figure 11.

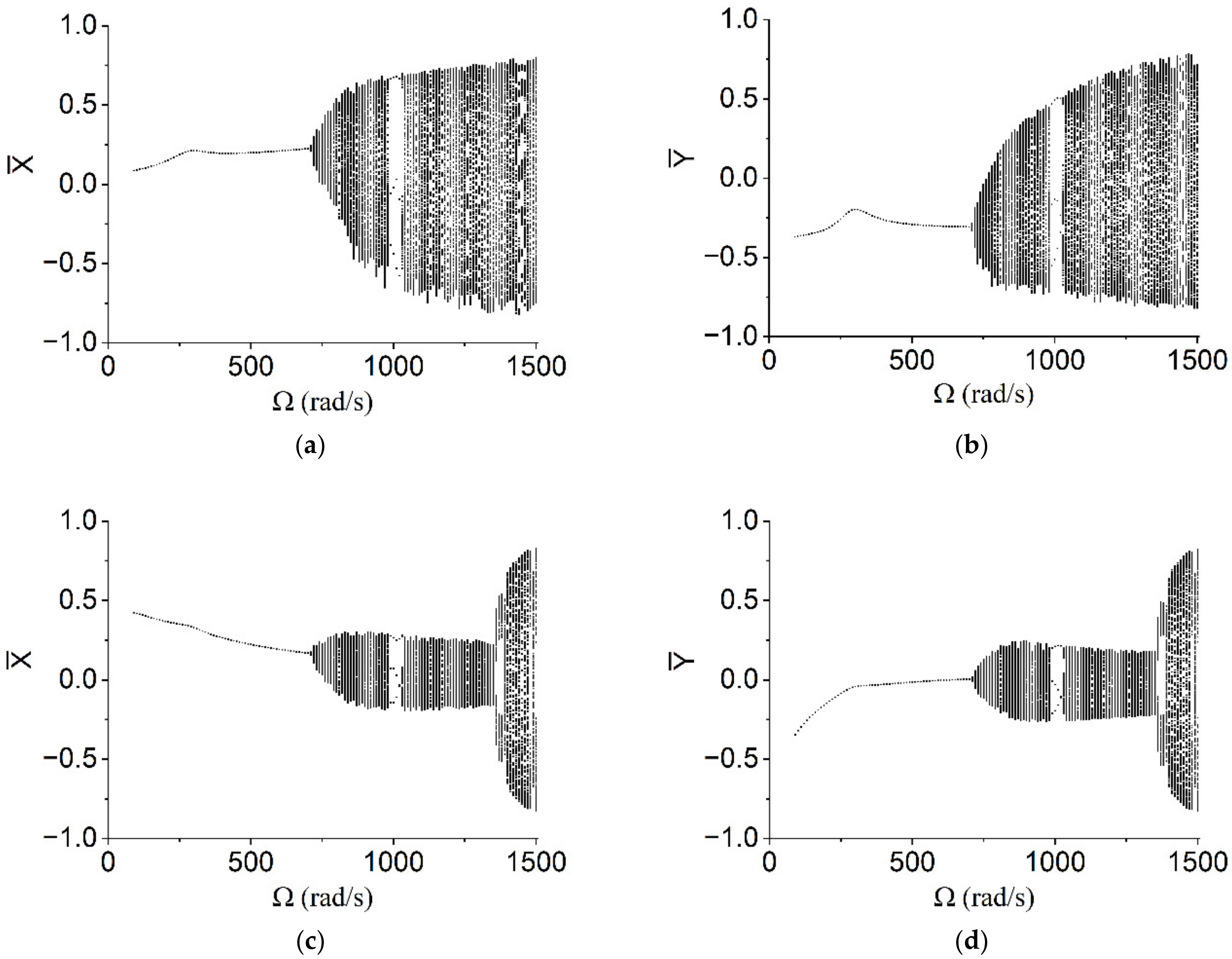

Figure 11. The bifurcation maps of Y-displacements of the traditional method: (**a**) X-displacement of rotor; (**b**) Y-displacement of rotor; (**c**) X-displacement of bearing; (**d**) Y-displacement of bearing.

The following conclusions can be seen from Figure 11:

(1) When $\Omega \in [90, 300]$ rad/s, the conclusion is same as item (1) in Figure 10. It can be identified that ω_n = 300 rad/s is the first-order critical speed of the rotor system;
(2) When $\Omega \in [710, 1350]$ rad/s, the bifurcation is observed and the amplitude value increases;
(3) When $\Omega \geq 1360$ rad/s, the amplitude of the bearing increases again substantially, with the maximum close to value 1.

The response of the rotor system in frequency has been investigated below. Two cascade maps of vertical displacement at the rotor and bearing of the VP method, respectively, are shown in Figure 12.

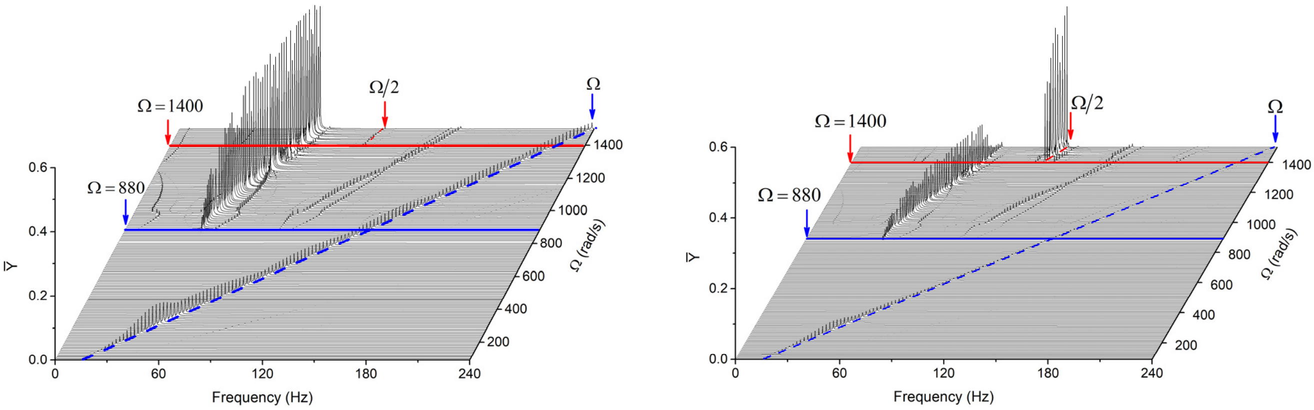

(**a**) (**b**)

Figure 12. Cascade maps of Y-displacements: (**a**) Rotor; (**b**) Bearing.

The following conclusions can be seen from Figure 12:

(1) When $\Omega \in [90, 870]$ rad/s, there is only the frequency component corresponding to the rotational speed (Ω) at the rotor and bearing;

(2) When $\Omega \in [880, 1500]$ rad/s, there are many frequency components at the rotor and bearing. When $\Omega \in [1400, 1500]$ rad/s, a half-frequency ($\Omega/2$) component of rotational speed appears at the rotor and bearing. In addition, the half-frequency component of the speed at the bearing is significantly higher than the peaks of the others that dominate. According to the literature [25], it can be judged that the oil film whirl occurred at the bearing, and Ω = 1400 rad/s is the oil film instability velocity of the rotor system.

The response of the rotor system in frequency in the traditional method has been investigated below. Two cascade maps of vertical displacement at the rotor and bearing, respectively, are shown in Figure 13.

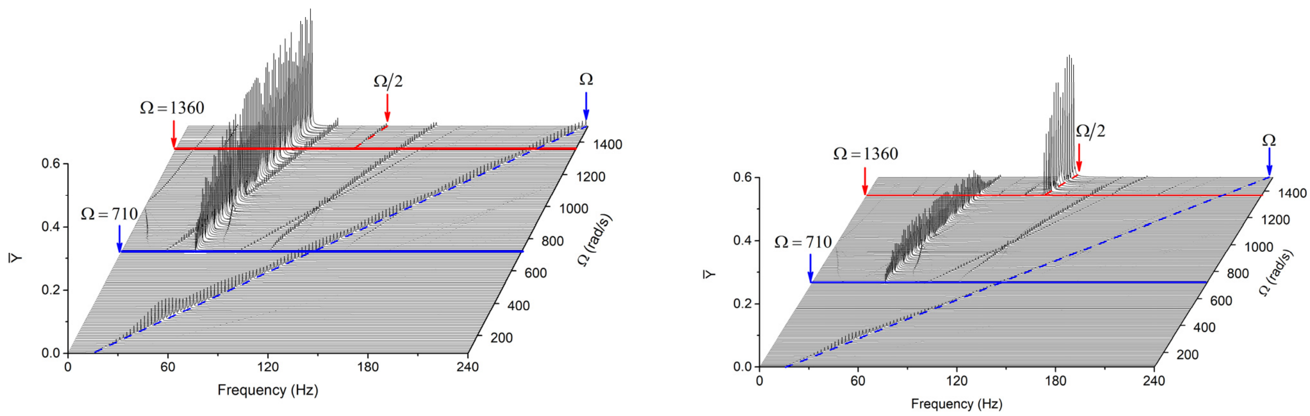

(**a**) (**b**)

Figure 13. Cascade maps of Y-displacements: (**a**) Rotor; (**b**) Bearing.

The following conclusions can be seen from Figure 13:

(1) When $\Omega \in [90, 700]$ rad/s, there is only the frequency component corresponding to the rotational speed (Ω) at the rotor and bearing;

(2) When $\Omega \in [710, 1500]$ rad/s, there are several frequency components at the rotor and bearing. It is worth noting that when $\Omega \in [1360, 1500]$ rad/s, the half-frequency ($\Omega/2$) of the rotational speed appears at the rotor and bearing. Furthermore, the half-frequency component at the bearing is obviously higher than the peaks of the

other frequency components that are dominant. According to the literature [25,26], it can be judged that the oil film whirl occurred at the bearing. Thus, Ω = 1360 rad/s is the oil film instability angular velocity of the rotor system.

The results of the varying parameters model are compared with those of the traditional constant model, as shown in Table 2. Although the first-order critical speeds are 300 rad/s for both the two methods, it also can be seen that the speed corresponding to the bifurcation point and the oil film instability angular velocity based on the traditional constant model are lower than those of the varying parameters model.

Table 2. Comparison of the results of the VP method and the traditional method (Unit: rad/s).

	The First-Order Critical Speed	Bifurcation Point	Oil Film Instability Angular Velocity
VP method	300	880	1400
Traditional constant method	300	710	1360

5.3. Axis Trajectories, Phase Diagrams and Poincaré Diagrams of the VP Method in Several Characteristic Speeds

In several speeds with obvious characteristics in Figure 10 (for example, first-order critical speed, bifurcation point and increasing point of bearing amplitude), the vertical (Y) dimensionless displacements of the rotor and the bearing, axis trajectories, phase diagrams, Poincaré diagrams of vertical displacement and velocity in Ω = 300, 880, 1250, 1330 and 1400 rad/s are shown in Figures 14–16, respectively.

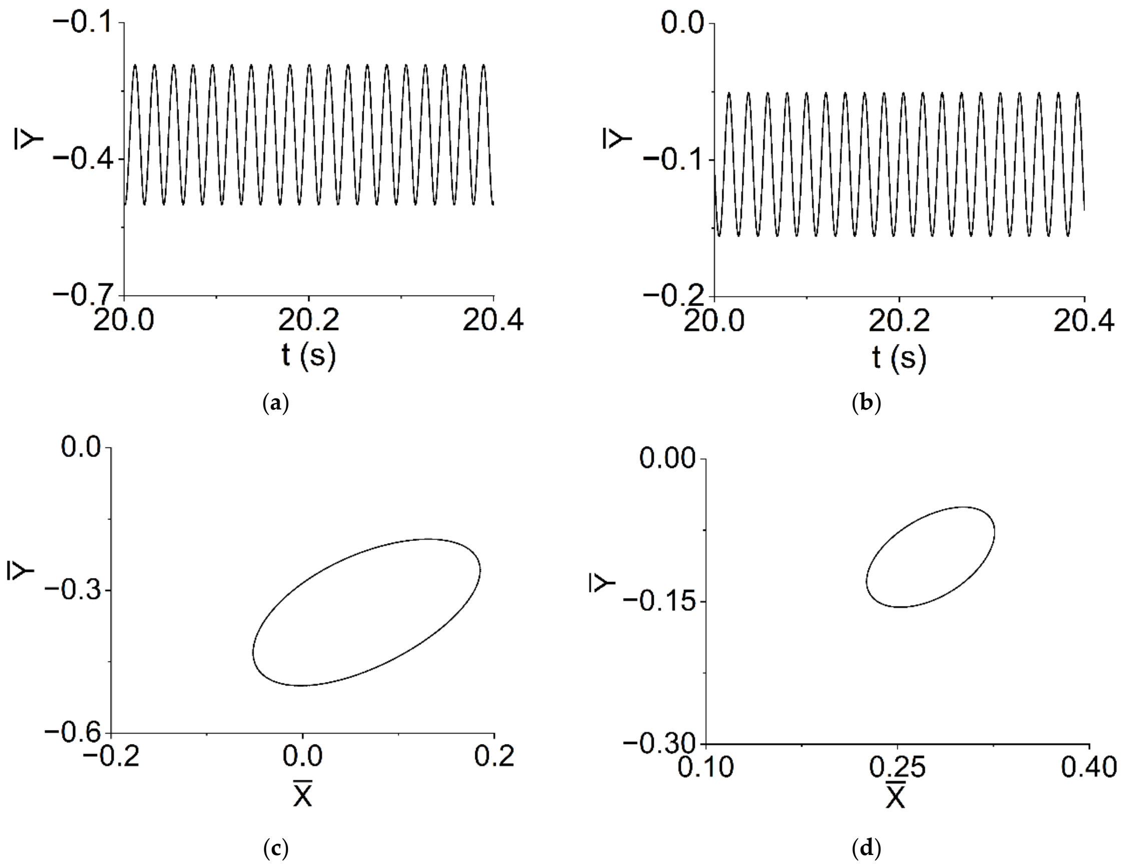

Figure 14. *Cont.*

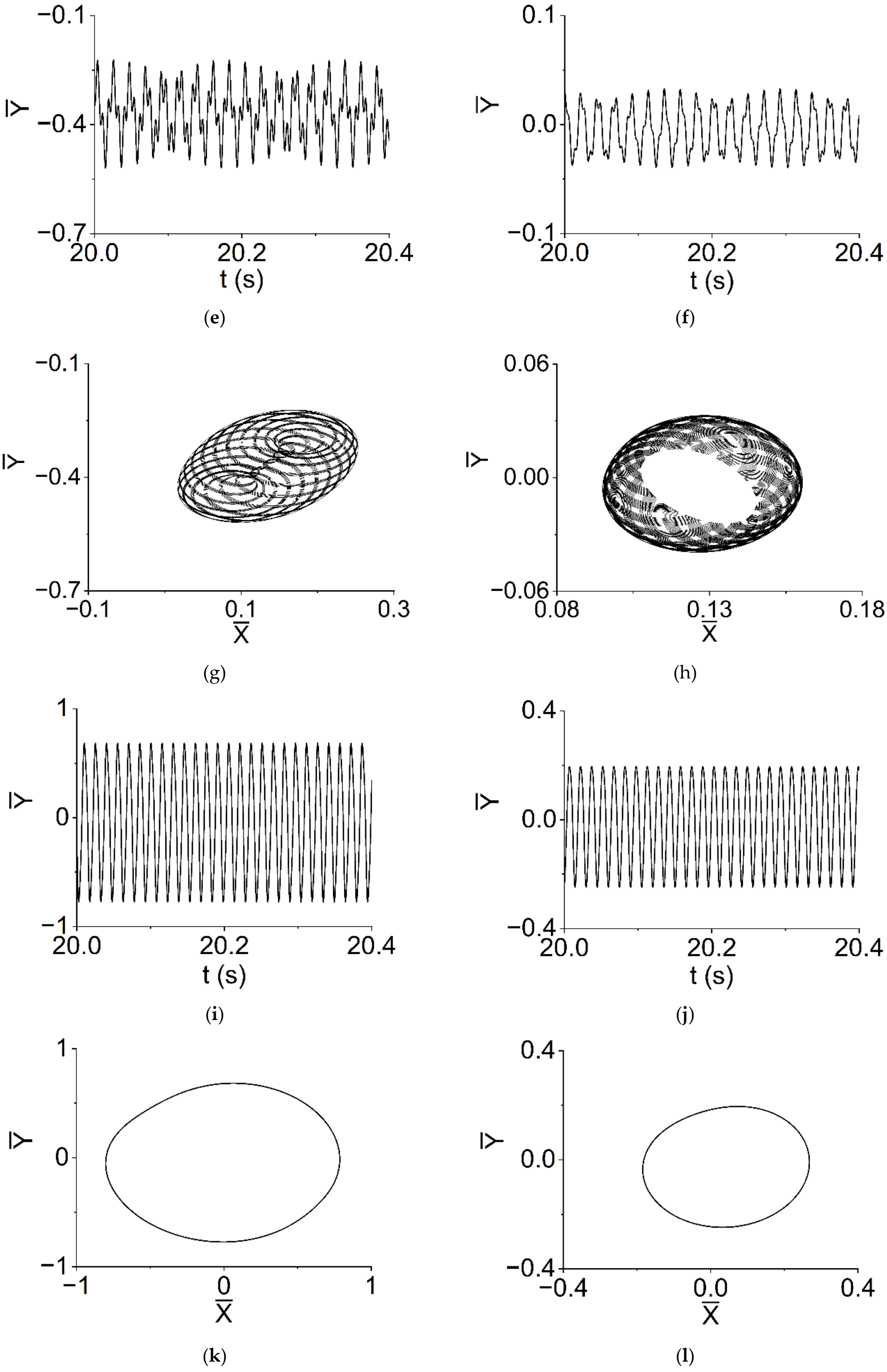

Figure 14. *Cont.*

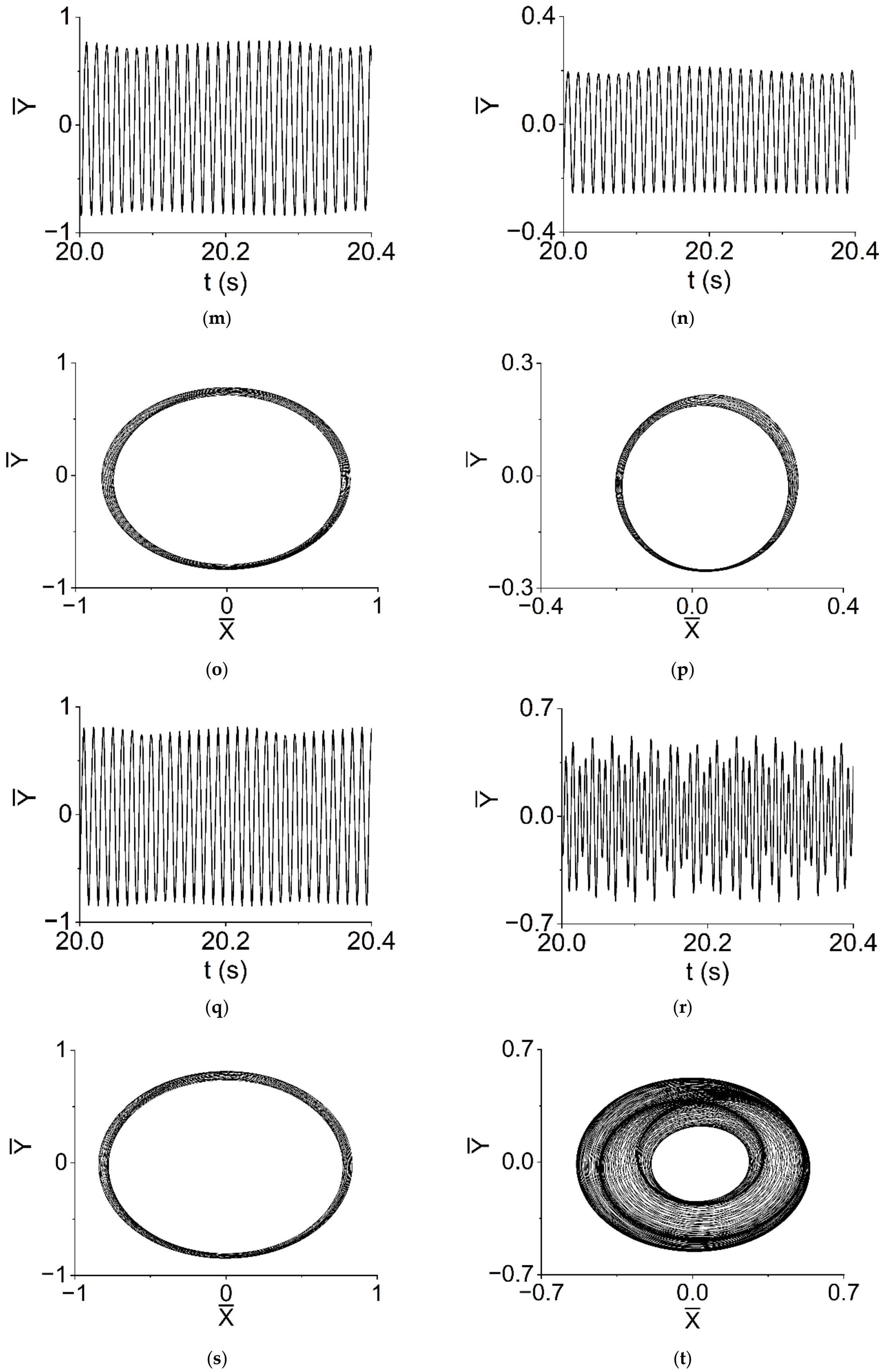

Figure 14. Y-displacements and trajectories of rotor system. (**a**) Y-displacement of rotor with $\Omega = 300$ rad/s, (**b**) Y-displacement of bearing with $\Omega = 300$ rad/s, (**c**) Trajectory of rotor with

Ω = 300 rad/s, (**d**) Trajectory of bearing with Ω = 300 rad/s, ®Y-displacement of rotor with Ω = 880 rad/s, (**f**) Y-displacement of bearing with Ω = 880 rad/s, (**g**) Trajectory of rotor with Ω = 880 rad/s, (**h**) Trajectory of bearing with Ω = 880 rad/s, (**i**) Y-displacement of rotor with Ω = 1250 rad/s, (**j**) Y-displacement of bearing with Ω = 1250 rad/s, (**k**) Trajectory of rotor with Ω = 1250 rad/s, (**l**) Trajectory of bearing with Ω = 1250 rad/s, (**m**) Y-displacement of rotor with Ω = 1330 rad/s, (**n**) Y-displacement of bearing with Ω = 1330 rad/s, (**o**) Trajectory of rotor with Ω = 1330 rad/s, (**p**) Trajectory of bearing with Ω = 1330 rad/s, (**q**) Y-displacement of rotor with Ω = 1400 rad/s, ®Y-displacement of bearing with Ω = 1400 rad/s, (**s**) Trajectory of rotor with Ω = 1400 rad/s, (**t**) Trajectory of bearing with Ω = 1400 rad/s.

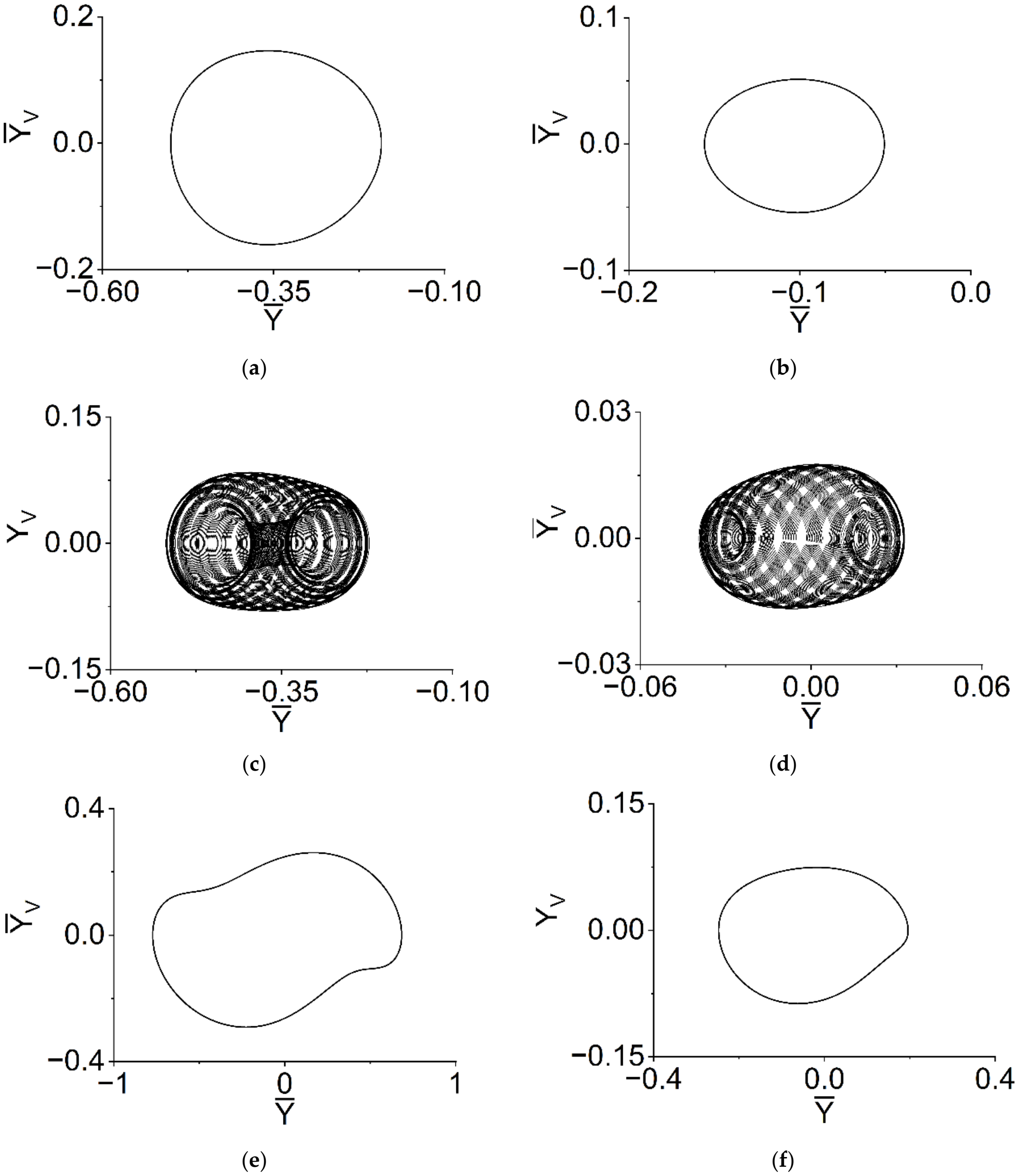

Figure 15. *Cont*.

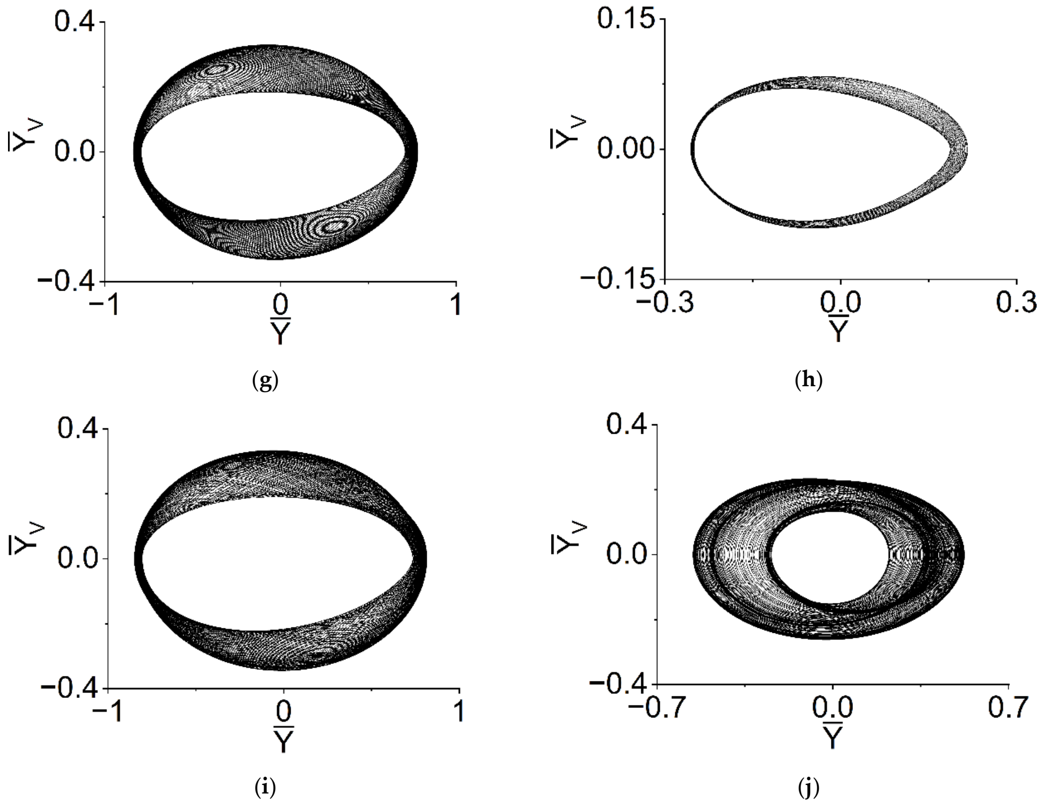

Figure 15. Phase maps of rotor system. (**a**) Rotor with Ω = 300 rad/s, (**b**) Bearing with Ω = 300 rad/s, (**c**) Rotor with Ω = 880 rad/s, (**d**) Bearing with Ω = 880 rad/s, I Rotor with Ω = 1250 rad/s, (**f**) Bearing with Ω = 1250 rad/s, (**g**) Rotor with Ω = 1330 rad/s, (**h**) Bearing with Ω = 1330 rad/s, (**i**) Rotor with Ω = 1400 rad/s, (**j**) Bearing with Ω = 1400 rad/s.

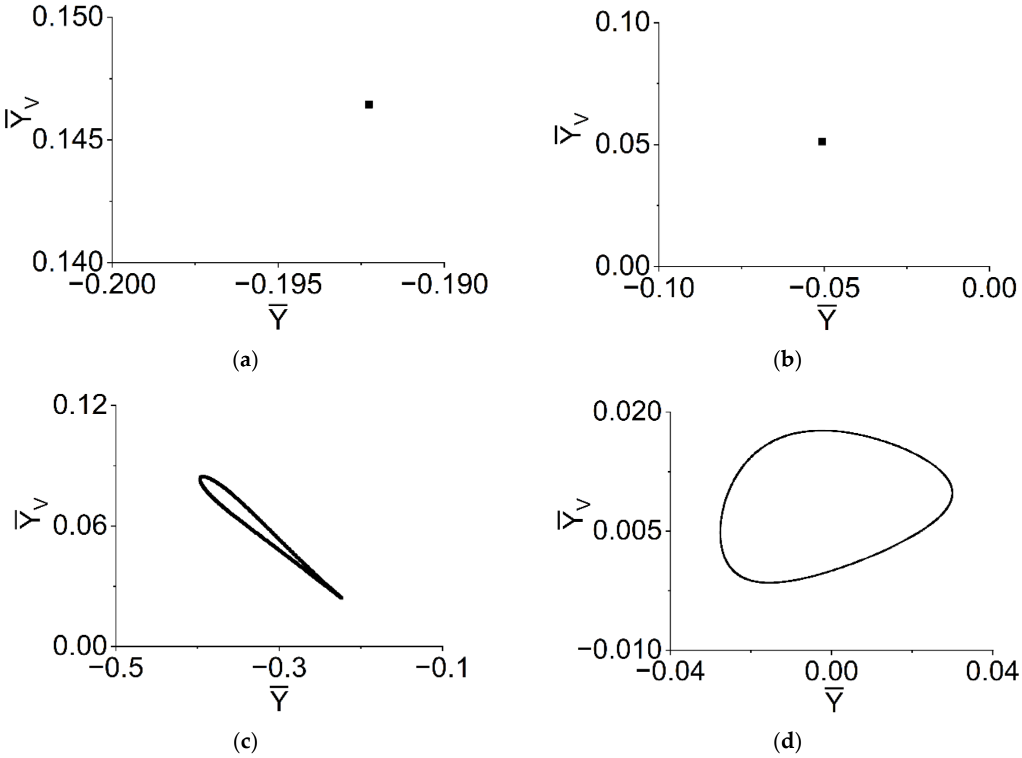

Figure 16. *Cont*.

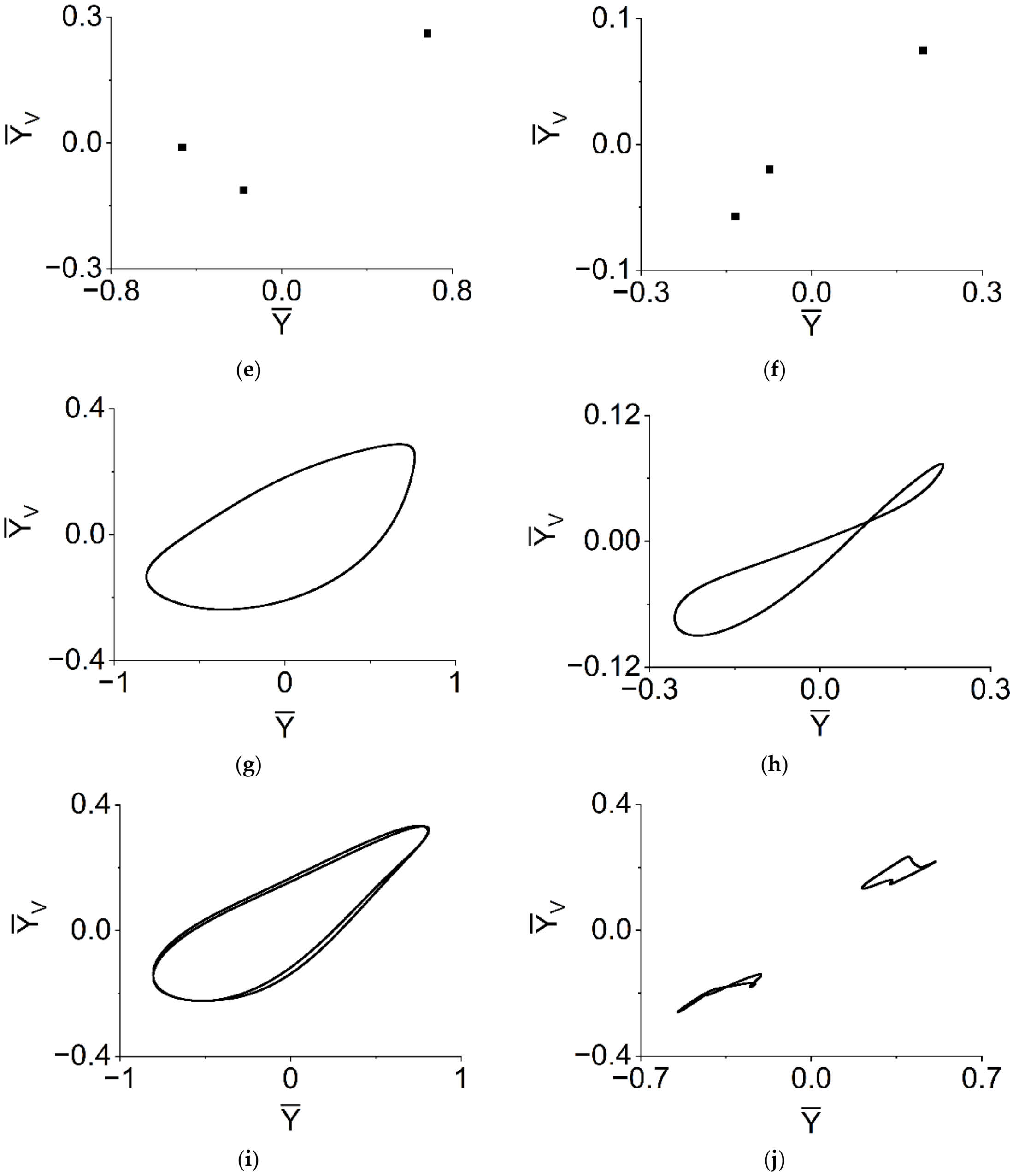

Figure 16. Poincaré maps of rotor system. (**a**) Rotor with Ω = 300 rad/s, (**b**) Bearing with Ω = 300 rad/s, (**c**) Rotor with Ω = 880 rad/s, (**d**) Bearing with Ω = 880 rad/s, (**e**) Rotor with Ω = 1250 rad/s, (**f**) Bearing with Ω = 1250 rad/s, (**g**) Rotor with Ω = 1330 rad/s, (**h**) Bearing with Ω = 1330 rad/s, (**i**) Rotor with Ω = 1400 rad/s, (**j**) Bearing with Ω = 1400 rad/s.

The following conclusions can be seen from Figures 14–16:

(1) When $\Omega \in [90, 300]$ rad/s, the periodic motion can be observed at rotor and bearings. The displacements of rotor and bearings are periodic; the shape of the trajectories and phases of rotor and bearings are a closed circle, respectively; there is only one point on each Poincaré map;

(2) When $\Omega \in [880, 1200]$ and $\Omega \in [1290, 1500]$ rad/s, the quasi-periodic motion can be obtained. The envelopes of displacements of rotor and bearings are periodic; the shapes of the trajectories and phases of rotor and bearings are quasi-periodic, respectively; most of the points on each Poincaré map formed a ring shape, while the shape in Figure 16h resembles a number eight;

(3) When $\Omega \in [1230, 1280]$ rad/s, both the rotor and the bearing have a three-fold period bifurcation. The displacements of rotor and bearings are periodic; the shape of the trajectories and phases of rotor and bearings are a closed circle, respectively; there are three isolated points on the Poincaré map (Ω = 1250 rad/s, as Figure 16e,f), which correspond to 1/3 harmonic of the system;

(4) When $\Omega = 1400$ rad/s, the envelopes of displacements of rotor and bearings are periodic; the shape of the trajectories and phases of rotor and bearings are quasi-periodic, respectively; the rupture of phase trajectory in the bearing can be observed, as in Figure 16j.

6. Conclusions

The rotordynamic characteristics of the rotor-bearing-seal system are determined by the nonlinear property of the bearings or seals. The Muszynska nonlinear seal force model is used to perform the simulations. Based on the CFD and RBF methods, approximate functional surfaces of the seal dynamic coefficients at different eccentricities and different speeds are obtained. Unlike the traditional constant method, the value of the varying parameters model that changes with the conditions in the transient calculation process is realized. The following conclusions can be drawn:

(1) The results of the first-order critical speed of the system are obtained by way of both the traditional constant model and the varying parameters model based on the approximate function surface method and the CFD method. The result obtained by the two methods is the same, which is equal to 300 rad/s;

(2) In the process of increasing the speed, the results of both models appeared to have quasi-periodic motion. The difference is that the speed corresponding to the bifurcation point based on the traditional constant model is lower than that of the varying parameters model;

(3) The oil film whirl phenomenon of the rotor-bearing-seal system is obtained by both algorithms. The difference is that the oil film instability angular velocity obtained based on the traditional constant model is lower than that of the varying parameters model. This means that the rotor-bearing-seal system in fact has a larger stable operation range.

Author Contributions: Conceptualization, R.W. and Y.W.; methodology, R.W.; software, R.W. and X.C.; validation, Y.W. and X.C.; formal analysis, R.W. and Y.W.; investigation, R.W.; resources, S.Y.; data curation, R.W. and X.C.; writing—original draft preparation, R.W.; writing—review and editing, Y.W. and R.W.; visualization, R.W. and X.C.; supervision, Y.W., S.Y. and X.G.; project administration, Y.W., S.Y. and X.G.; funding acquisition, S.Y. All authors have read and agreed to the published version of the manuscript.

Funding: This research was funded by the National Natural Science Foundation of China (Grant U1808214 and U1908217) and the Industry—Education Fusion Project by the Bureau of Education of Liaoning Province for their sponsorships.

Data Availability Statement: Not applicable.

Conflicts of Interest: The authors declare no conflict of interest.

References

1. Black, H.F. Effects of Hydraulic Forces in Annular Pressure Seals on the Vibrations of Centrifugal Pump Rotors. *J. Mech. Eng. Sci.* **1969**, *11*, 206–213. [CrossRef]
2. Childs, D.W. Dynamic Analysis of Turbulent Annular Seals Based on Hirs' Lubrication Equation. *J. Lubr. Technol.* **1983**, *105*, 429–436. [CrossRef]
3. Childs, D.W. Finite-Length Solutions for Rotordynamic Coefficients of Turbulent Annular Seals. *J. Lubr. Technol.* **1983**, *105*, 437–445. [CrossRef]
4. Childs, D.W.; Scharrer, J.K. An Iwatsubo-Based Solution for Labyrinth Seals Comparison to Experimental Results. *J. Eng. Gas Turbines Power-Trans. ASME* **1986**, *108*, 325–331. [CrossRef]

5. Childs, D.W.; Wade, J. Rotordynamic-Coefficient and Leakage Characteristics for Hole-Pattern-Stator Annular Gas Seals-Measurements versus Predictions. *J. Tribol.-Trans. ASME* **2004**, *126*, 326–333. [CrossRef]
6. Childs, D.W.; McLean, J.; Zhang, M.; Arthur, S. Rotordynamic Performance of a Negative-Swirl Brake for a Tooth-on-Stator Labyrinth Seal. *J. Eng. Gas Turbines Power ASME* **2016**, *138*, 062505. [CrossRef]
7. Nelson, C.C. Comparison of Hirs' Equation with Moody's Equation for Determining Rotordynamic Coefficients of Annular Pressure Seals. *J. Tribol.-Trans. ASME* **1987**, *109*, 144–148. [CrossRef]
8. Muszynska, A. Whirl and Whip–Rotor Bearing Stability Problems. *J. Sound Vib.* **1986**, *110*, 443–462. [CrossRef]
9. Bently, D.E.; Muszynska, A. *Role of Circumferential Flow in the Stability of Fluid Handling Machine Rotors*; Bently Rotor Dynamics Research Corporation: Minden, NV, USA, 1989; pp. 415–430.
10. Muszynska, A.; Bently, D.E.; Franklin, W.D.; Grant, J.W.; Goldman, P. Applications of Sweep Frequency Rotating Force Perturbation Methodology in Rotating Machinery for Dynamic Stiffness Identification. *J. Eng. Gas Turbines Power-Trans. ASME* **1993**, *115*, 266–271. [CrossRef]
11. Li, S.T.; Xu, Q.Y.; Zhang, X.L. Nonlinear Dynamic Behaviors of a Rotor-Labyrinth Seal System. *Nonlinear Dyn.* **2007**, *47*, 321–329. [CrossRef]
12. Wang, Y.F.; Wang, X.Y. Nonlinear Vibration Analysis for a Jeffcott Rotor with Seal and Air-Film Bearing Excitations. *Math. Probl. Eng.* **2010**, *2010*, 657361. [CrossRef]
13. Zhang, E.Z.; Jiao, Y.H.; Chen, Z.B. Dynamic behavior analysis of a rotor system based on a nonlinear labyrinth-seal forces model. *J. Comput. Nonlinear Dyn.* **2018**, *13*, 101002. [CrossRef]
14. Xu, Q.; Luo, Y.; Yao, H.; Zhao, L.; Wen, B. Eliminating the Fluid-Induced Vibration and Improving the Stability of the Rotor/Seal System Using the Inerter-Based Dynamic Vibration Absorber. *Shock. Vib.* **2019**, *2019*, 1–9. [CrossRef]
15. Zhang, K.; Jiang, X.; Li, S.; Huang, B.; Yang, S.; Wu, P.; Wu, D. Transient CFD Simulation on Dynamic Characteristics of Annular Seal under Large Eccentricities and Disturbances. *Energies* **2020**, *13*, 4056. [CrossRef]
16. Mutra, R.R.; Srinivas, J. Parametric design of turbocharger rotor system under exhaust emission loads via surrogate model. *J. Braz. Soc. Mech. Sci. Eng.* **2021**, *43*, 1–17. [CrossRef]
17. Moore, J.J. Three-Dimensional CFD Rotordynamic Analysis of Gas Labyrinth Seals. *J. Vib. Acoust.* **2003**, *125*, 427–433. [CrossRef]
18. Li, Z.; Chen, Y.; Chen, Z.; Jiao, Y.; Ma, W. Nonlinear Dynamic Characteristics Analysis of the Gas Exciting Force in the Rotor-Seal System. *J. Dyn. Control* **2013**, *11*, 126–132. (In Chinese)
19. Luo, Y.; Wang, P.; Jia, H.; Huang, F. Dynamic Characteristics Analysis of a Seal-Rotor System with Rub-Impact Fault. *J. Comput. Nonlinear Dyn.* **2021**, *16*, 081003. [CrossRef]
20. Menter, F.R. Two-equation eddy-viscosity turbulence models for engineering applications. *Aiaa J.* **1994**, *32*, 1598–1605. [CrossRef]
21. Hirano, T.; Guo, Z.L.; Kirk, R.G. Application of Computational Fluid Dynamics Analysis for Rotating Machinery—Part II Labyrinth Seal Analysis. *J. Eng. Gas Turbines Power-Trans. ASME* **2005**, *127*, 820–826. [CrossRef]
22. Wang, Z.H.; Xu, L.Q.; Xi, G. Numerical Investigation on the Labyrinth Seal Design for a Low Flow Coefficient Centrifugal Compressor. In Proceedings of the ASME Turbo Expo 2010: Power for Land, Sea, and Air. Volume 7: Turbomachinery, Parts A, B, and C, Glasgow, UK, 14–18 June 2010; ASME; pp. 2031–2041.
23. Zhang, H.X.; Huang, W.Q.; Wang, Y.; Lu, L.; Lyu, S. Research on Meshfree Method for Analyzing Seal Behavior of a T-DGS. *Int. J. Precis. Eng. Manuf.* **2017**, *18*, 529–536. [CrossRef]
24. Wang, R.; Guo, X.L.; Wang, Y.F. Nonlinear analysis of rotor system supported by oil lubricated bearings subjected to base movements. *Proc. Inst. Mech. Eng. Part C J. Mech. Eng. Sci.* **2016**, *230*, 543–558. [CrossRef]
25. Muszynska, A. Stability of Whirl and Whip in Rotor/Bearing Systems. *J. Sound Vib.* **1988**, *127*, 49–64. [CrossRef]
26. Cheng, M.; Meng, G.; Jing, J.P. Non-linear dynamics of a rotor-bearing-seal system. *Arch. Appl. Mech.* **2006**, *76*, 215–227. [CrossRef]